Experimental and Theoretical Assessment of Mechanical and Optical Effects in Nonuniformly Heated IR Windows

Donald D. Duncan, Kevin C. Baldwin, David W. Blodgett, Michael J. Elko, Richard I. Joseph, Mark J. Mayr, Daniel T. Prendergast, David H. Terry, Michael E. Thomas, and Suzanne C. Walts

This article discusses a series of optical techniques for assessing the performance of heated IR windows. The assessment considers the complete thermo-mechanical behavior as well as the boresight error and image quality of the sensor that looks through the window. The entire discussion serves as a vehicle for emphasizing the role that fundamental research plays in the everyday mission of APL. We demonstrate that research into the fundamental properties of matter not only provides insight into the behavior of the material, but often leads to the creation of secondary tools or procedures that in turn can be used to assess system performance.

INTRODUCTION

Many optical guidance sensors view the outside world through a protective window of some kind. These windows, which are typically either flat or hemispherical (dome) in shape, are not merely an adjunct to the system but rather an integral component. The nominal properties of these windows are taken into consideration in the optical design of the overall sensor. For missile applications, certain flight conditions affect these windows (through aerodynamic heating) and hence the imaging performance of the sensor. Subsequently, this change in optical performance affects the guidance of the vehicle in a dynamic sense. Boresight error is an example: Is the target where the sensor thinks it is? The issues become more complicated still, because certain aspects of flight (altitude, speed, angle of attack) affect the thermo-mechanical impact on the window. Obviously, for a sensor that is actively guiding the vehicle's flight, the dependence of this boresight error on viewing angle is of critical importance. For these reasons, much effort has gone into computer engagement models that incorporate all optical and mechanical aspects of the vehicle/target interaction.

At present, characterization of the performance of the optical sensor is done "off-line" because it is very numerically intensive (Fig. 1). Based on certain nominal flight trajectories, an empirical engineering model estimates the aerothermal heat loads on the window surface. A finite-element thermal model, ATLAS,[1] uses these surface temperature estimates to predict the spatio-temporal temperature distribution $T(r, t)$ throughout the volume of the window. Given this volumetric thermal distribution, NASTRAN,[2] a finite-element code,

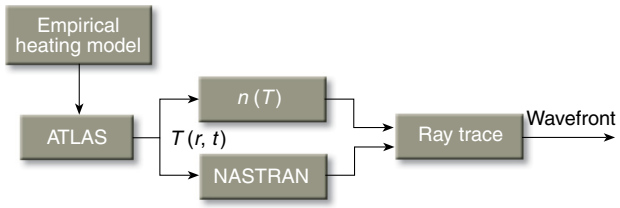

Figure 1. Current numerical simulation procedure.

calculates stress distributions and deformations of the window. Finally, numerical ray trace codes are used to predict the optical performance of the system, which includes the window as a component. These ray trace codes use deformation predictions made by NASTRAN and the temperature-dependent refractive index $n(T)$ profile within the window to provide detailed information on the point-spread function from which the boresight error and image blur can be obtained.

Each stage of this process has potential for error and oversight and, owing to its complexity, little insight is provided into the phenomena directly affecting sensor performance. As a result, each component of this performance prediction model must be verified experimentally. Validation of this complex performance prediction procedure, however, is merely an intermediate step toward the final goal, i.e., the creation of an accurate parametric system performance model that captures the physics of the problem and is efficient enough to serve as a component of a detailed weapon system engagement model.

The genesis of the APL Electro-Optical Systems Group's role in these efforts was our interest in what may be called materials science—the study of the fundamental properties of matter. In many cases, this research has led to the development of tools and procedures that fall into the category of nondestructive evaluation (NDE). Particular applications of these NDE tools might be considered test and evaluation efforts. Others may prove useful in production proof testing of the windows themselves (process control). In short, our efforts span the spectrum from fundamental research to applications of direct and significant impact on a number of Navy programs. We illustrate in this article the importance of such fundamental research and its relevance to current APL programs. Furthermore, we stress that research of this nature is not strictly a precursor to applied work, but by its very nature must proceed concomitantly.

EXPERIMENTAL TOOLS

Through our research into the opto-mechanical properties of materials, we have developed a wide variety of tools for the test and evaluation of infrared (IR) windows and materials. In these efforts, we have used traditional tools of the trade (spectroscopy, interferometry, radiometry) in novel ways as well as more modern tools such as laser-based ultrasonics. We describe several of these techniques that have led to a series of NDE procedures. Subsequently, we discuss the application of these techniques to the evaluation and performance modeling of IR windows.

Fundamental Material Properties Research Tools

These tools are of a more fundamental nature and form the basis for many of the NDE techniques that we discuss here. Laser-based ultrasonics (LBU) provides a means of assessing the elastic moduli of dielectric materials at elevated temperatures; interferometric techniques yield information on thermal effects on the refractive index; polarimetry provides information on stress-induced birefringence; and spectroscopic techniques provide emissivity data.

Laser-Based Ultrasonics—Elastic Moduli

As the name suggests, the elastic modulus of a material can be thought of as a parameter similar to that of the restoring constant of a spring. It relates the amount of strain (deformation) that a material will experience when placed under a particular stress (force). Thus, knowledge of the elastic modulus is important for understanding how the material will respond to mechanical loads or thermal gradients. Of particular interest is the behavior of the modulus as a function of temperature, since this enables prediction of the stress levels within a sensor window as it is heated during flight. An isotropic material has two distinct moduli, one each for compression and shear; a crystalline material, depending on its symmetry properties, may have as many as 21.

We measure elastic moduli using LBU,[3,4] a noncontact, nondestructive testing technique (Fig. 2). In this procedure a short laser pulse (typically on the order of a few nanoseconds) is focused on the sample of interest. By choosing an optical wavelength that is strongly absorbed by the material, the incident pulse energy results in a sudden localized thermal expansion. The effect is similar to what would be expected from a mechanical impact: a traveling acoustic wave is generated which propagates through the sample to the opposite side, where it produces a very small deformation in the surface (a few nanometers). A stabilized laser interferometer is used to detect this deformation. Knowledge of the sample thickness and the propagation time yields an estimate of the velocity v which in general is related to the appropriate elastic modulus C by

$$C = v^2 \rho , \qquad (1)$$

where ρ is the density of the material. In the thermoelastic regime no damage occurs to the specimen, thus the term "nondestructive." Because of the short

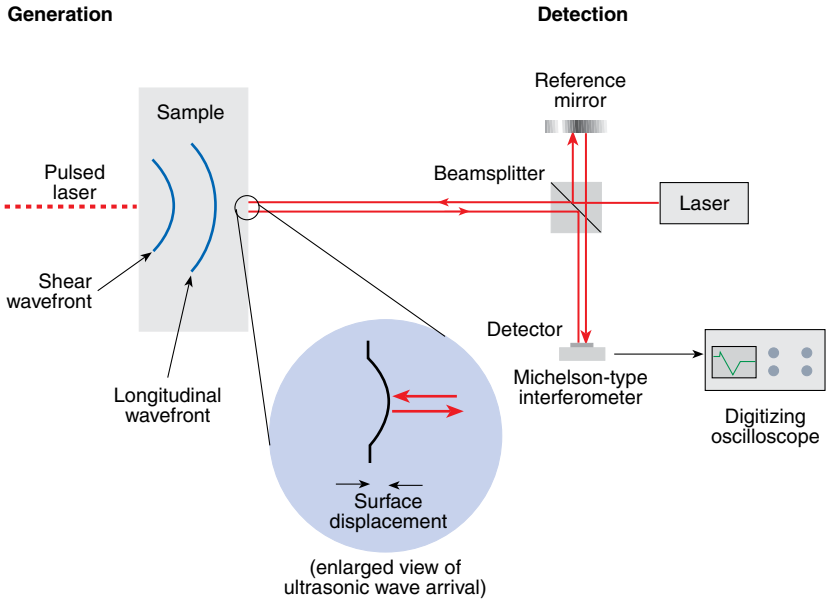

Figure 2. Concept of laser-based ultrasound generation and detection.

duration of the generation laser pulse, the arrival time of the ultrasound can be measured very accurately. The method is termed "ultrasonic" because the excitation pulse is sufficiently short that a very high frequency acoustic wave is produced.

To measure the temperature dependence of the elastic modulus, the sample is placed in a high-temperature tube furnace. This device, which provides optical access to the sample for the excitation laser beam and the interferometer probe beam, can achieve stable temperatures approaching 1700°C.

Applying LBU to the determination of the elastic moduli of sapphire (the material of choice for missile applications) presents several challenges. Single-crystal sapphire is a mechanically anisotropic material, characterized by six distinct elastic moduli.[5] To determine all six moduli, measurements are made on four samples that are cut along specific crystallographic orientations. Sapphire is transparent across a large portion of the spectrum, from visible to mid-wave IR (MWIR) wavelengths, but absorbs very strongly at 10.6 μm. Therefore, a pulsed transversely excited atmospheric-pressure CO_2 laser is used to generate the ultrasound.

Example LBU-measured waveforms are shown in Fig. 3, each for a different crystallographic orientation. The longitudinal and shear wave arrivals are marked on the *c*-axis sample, with similar wave arrivals visible on the three remaining samples. Collecting and analyzing these waveforms as a function of temperature led to the elastic moduli estimates, as calculated from Eq. 1 and shown in Fig. 4. As seen here, results obtained using LBU for C_{11}, one of sapphire's six elastic moduli, are in excellent agreement with previously published values.[6]

Besides our interest in sapphire, we are also using LBU to measure the thermo-mechanical properties of other candidate window materials such as AlON and spinel.[7] Measurements of this type also can provide insight into the impact of treatments, such as the introduction of defects[8] to impede possible fracture.

Optical Interferometry—Refractive Index

Precise measurements of the temperature dependence of the IR refractive index are crucial for predicting boresight error and image blur through nonuniformly heated windows. One of the most important pieces of information is the derivative of the refractive index with respect to temperature; i.e., the thermo-optic coefficient. A variety of methods exist for determining the refractive index of solids. We have chosen to use a laminar sample with highly parallel surfaces and measure the interference pattern between directly transmitted and internally reflected light. In effect, the sample acts as a solid etalon.[9] Interference produces intensity modulation, with maxima occurring when the optical path length difference between the two paths is an integer number of wavelengths,

$$m\lambda = 2L(T)n(\lambda, T) \ , \qquad (2a)$$

where λ is the wavelength, L is the sample thickness, T is the temperature, and n is its refractive index. Alternatively, one can express this relationship in terms of wavenumber ν,

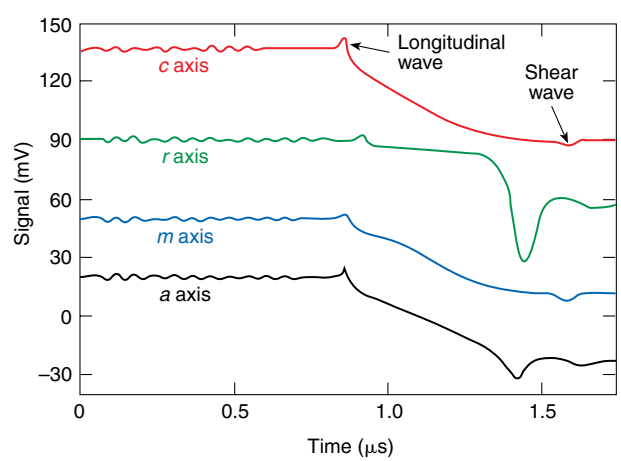

Figure 3. Example ultrasonic waveforms.

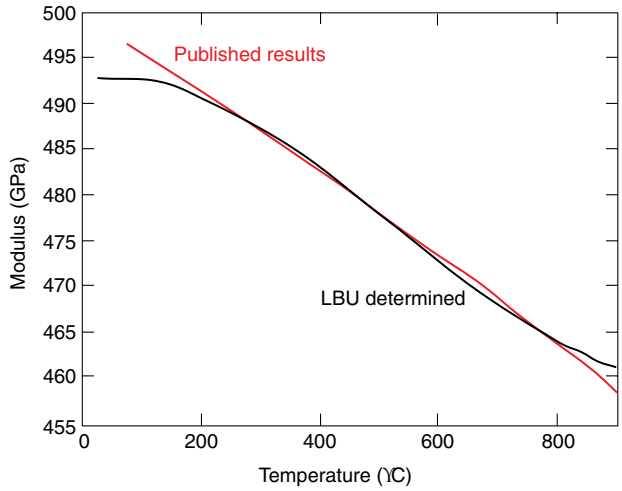

Figure 4. Comparison of measured and published[6] results for C_{11}.

$$m = 2L(T)n(\nu,T)\nu\ . \tag{2b}$$

The separation between maxima is called the free spectral range Δ, which is related to the refractive index (assuming small Δ) by

$$\frac{1}{2L(T)\Delta(\nu,T)} = n(\nu,T) + \nu\frac{dn(\nu,T)}{d\nu} = \frac{d[n(\nu,T)\nu]}{d\nu}\ . \tag{3}$$

High spectral resolution measurements are used to determine peak locations and hence free spectral range. Our method of determining refractive index from these free spectral range data is based on the integration of Eq. 3 between some reference wavenumber ν_0 and the wavenumber of interest,

$$n(\nu,T) + \frac{1}{\nu}\left[\nu_0 n(\nu_0,T) - \frac{p(\nu,T)}{2L(T)}\right], \tag{4}$$

where p is the number of maxima between ν_0 and ν. Our method is insensitive to noise in the data because we do not need to know the exact *location*, just the *number* of peaks lying between ν_0 and ν. We use a BOMEM Fourier transform spectrometer to make these transmission measurements. The spectrometer is configured to cover the spectral ranges of 1800 to 6000 cm^{-1} and 4000 to 10,000 cm^{-1}. Measurements are made from room temperature (300 K) to 1000 K at APL and from 10 to 600 K at the National Institute of Standards and Technology (NIST).

Accurate determination of $n(\nu,T)$ further requires detailed knowledge of $L(T)$ and $n(\nu_0,T)$. Published data on the thermal expansion[7] are used to determine the temperature dependence of the thickness of the sample along the c axis. The refractive index at the reference wavenumber is also obtained from the literature.[7]

Figure 5 shows the experimental estimates of the refractive index as a function of temperature below and above room temperature at 1 μm (10,000 cm^{-1}), 1.7 μm (6000 cm^{-1}), 2.5 μm (4000 cm^{-1}), and 4 μm (2500 cm^{-1}). As seen here, results match well in the temperature range where NIST and APL experiments overlap.

Polarimetry—Stress–Optic Properties

Photo-elastic analysis is a well-established technique that provides a powerful means of experimentally measuring full-field, real-time stress distributions in a test article having known photo-elastic properties.[10] Commonly chosen materials are optically isotropic but exhibit a stress-induced change in refractive index, making them artificially birefringent (i.e., the refractive index varies with orientation of the electric field). These changes in refractive index are directly proportional to the applied stress. As a result, measurement of the induced birefringence, together with knowledge of the stress–optic coefficients (which relate the change in refractive index to the applied stress), allows one to infer the stresses in the model.

Naturally birefringent crystalline materials have refractive indices that vary with crystallographic orientation. For uniaxial materials, such as sapphire, there are two distinct indices of refraction known as the ordinary n_o and extraordinary n_e. As with optically isotropic materials, sapphire exhibits an induced birefringence that is proportional to the applied stress.

Stress-induced birefringence can be measured using either a linear or circular polariscope. A linear polariscope provides information on both the principal stress

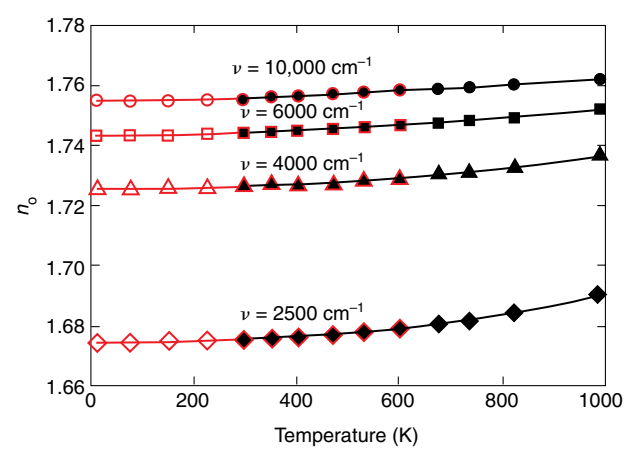

Figure 5. Experimental estimates of the refractive index of o-ray sapphire n_o from NIST (red) and APL (black).

differences and the principal stress directions in the test specimen, whereas a circular polariscope provides information only on the principal stress differences. Lines of principal stress differences and principal stress directions are manifested as two sets of fringes, termed isochromatic and isoclinic, respectively.

The experimental configuration for a plane polariscope is shown in Fig. 6. Ours consists of an unpolarized light source (HeNe laser, $\lambda = 632.8$ nm), a beam expander, a linear polarizer, the test specimen, an analyzer (another linear polarizer with the optical axis aligned either parallel or perpendicular to the first linear polarizer), and a viewing screen. The resulting fringe pattern is imaged with a CCD camera and captured at a rate of 10 Hz for subsequent analysis.

IR Spectroscopy—Spectral Emissivity

The spectral radiance of a material, $L_M(\theta, \nu, T)$, is defined as the flux per unit projected area per unit solid angle per unit wavenumber, typically W/(m^2 sr cm^{-1}), and is expressed as

$$L_M(\theta, \nu, T) = \varepsilon_\nu(\theta, T) L_{BB}(\nu, T) , \qquad (5)$$

where $\varepsilon_\nu(\theta, T)$ is the spectral emissivity of the material, $L_{BB}(\nu, T)$ is the spectral radiance of a blackbody, and θ is the angle of emission (i.e., the angle between the surface normal and the emitted ray). In general, the emissivity is composed of two portions, one specular and one diffuse. Since the materials in which we are interested have smooth, flat surfaces and negligible bulk scattering, the diffuse component is negligible.

Based on the total power law and Kirchhoff's law of radiation, the specular component of directional near-normal emissivity can be expressed as

$$\varepsilon_\nu(\theta, T) = \frac{(1 - R(\nu, \theta, T))(1 - \exp[-\beta_a(\nu, T)L/\cos\theta])}{1 - R(\nu, \theta, T)\exp[\beta_a(\nu, T)L/\cos\theta]} , \qquad (6)$$

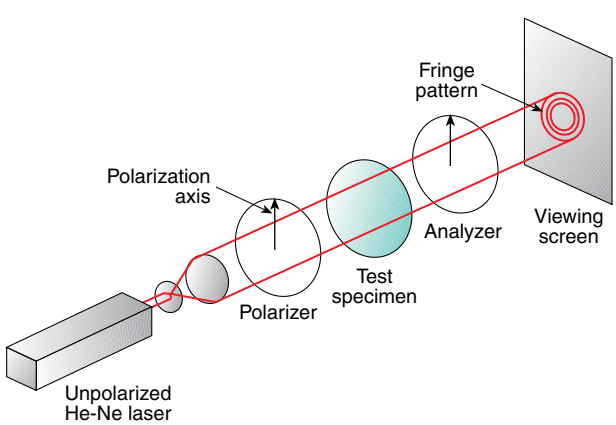

Figure 6. Conceptual design of a plane polariscope.

where $R(\nu, \theta, T)$ is the single-surface Fresnel reflection coefficient, β_a is the absorption coefficient, and L is the sample thickness. The magnitude of the single-surface reflectance $|R|$ of a medium (at normal incidence) is

$$|R(\nu, T)| = \left| \frac{\boldsymbol{n}(\nu, T) - 1}{\boldsymbol{n}(\nu, T) + 1} \right|^2 , \qquad (7)$$

where the complex index of refraction $\boldsymbol{n}$ is composed of a real part n and an imaginary part k (the index of extinction),

$$\boldsymbol{n}(\nu, T) = n(\nu, T) - jk(\nu, T) , \qquad (8)$$

and the absorption coefficient is related to this imaginary component through the formula

$$\beta_a(\nu, T) = 4\pi\nu k(\nu, T) . \qquad (9)$$

For temperatures below 1000 K, it is best to determine emittance from reflectance and transmittance measurements. Emittance is obtained either by applying the total power law or by determining $|R(\nu, \theta, T)|$ and β_a and then applying Eq. 6. For temperatures above 1000 K, it is best to determine emittance directly from emissometer measurements. This has been our approach for the past 15 years.[11] The result is an optical properties measurement capability that spans the range from room temperature to 2000 K. Using Eq. 6, along with n and k values calculated with one-phonon and multiphonon models developed at APL,[12] we can generate theoretical emissivity curves. An example comparison between theoretical emissivity and the experimental data is shown in Fig. 7. The emissivity model is used to model the elevated background radiance of a hot window for IR sensor applications.

Applications of NDE Tools

We now illustrate how a number of our research efforts have led to the development of important NDE tools and procedures. As an example, the spectroscopic studies of thermal emission have provided the capability of performing imaging pyrometry. Polarimetric properties are important in assessing the stress-induced properties of optical windows. Finally, interferometric techniques are useful in assessing the performance of optical systems.

Imaging Pyrometry

APL has developed methods of measuring the surface temperatures of oxide window materials, viz. sapphire (Al_2O_3), by using a long-wave IR (LWIR) mercury-cadmium-telluride (MCT) camera.[13,14] This camera provides spatially resolved (400 × 800 pixels) measurements of the temperature of a sapphire window as

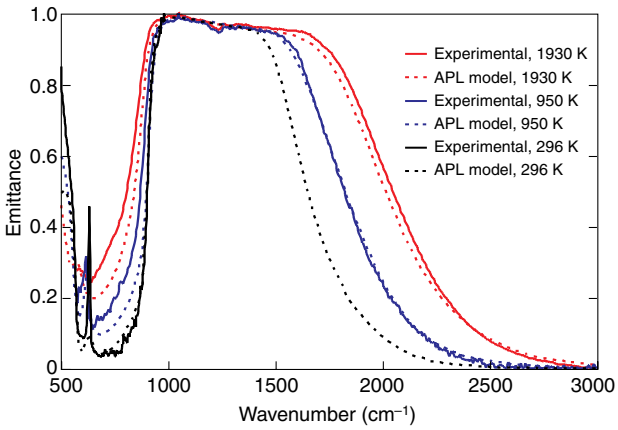

Figure 7. Comparison of experimental and theoretical estimates of emissivity.

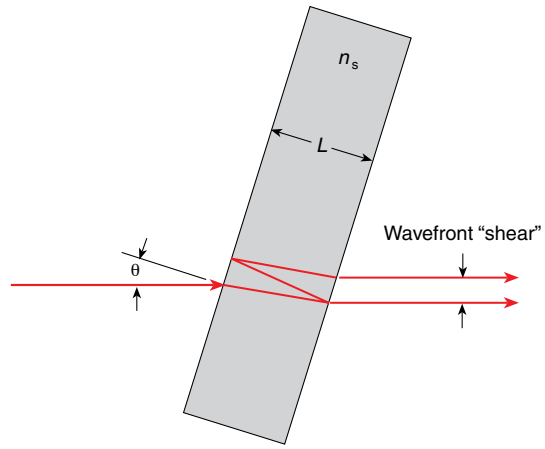

Figure 8. Concept of a shearing interferometer (amount of shear $s = L\sin(2\theta)/(n_s^2 - \sin^2\theta)^{1/2}$, n_s = refractive index, L = thickness, and θ = tilt of dielectric plate).

it undergoes heating. With the appropriate processing, these images provide radiometrically calibrated temperature maps of the outer surface. The pyrometry system has been used for aerothermal sapphire dome heating measurements in APL's wind tunnels and for a series of CO_2 laser-heating tests that we shall discuss shortly. The key optical properties that make LWIR imaging pyrometry of sapphire possible are sapphire's near blackbody emittance in the LWIR band (7.4 to 11.7 μm), the near temperature independence of the emittance (see Fig. 7), and the relatively constant directional emissivity over angles from 0° to 60°.

Special precautions are required for imaging pyrometry in the presence of laser heating. To minimize the possibility of stray radiation directly from the CO_2 laser, which would contaminate the measurements, a special notch absorption filter using SF_6 gas is employed. Of course calibration of the camera with this ancillary filtering (SF_6 cell) component is required. This is accomplished by imaging a blackbody over the temperature range of 50° to 1000°C in 50°C intervals. At each temperature, the average number of counts is determined over the center of the blackbody image. The measured LWIR camera counts are then converted to radiance by means of a linear least squares fit. The last step is to compute the temperature by curve-fitting the relation between the normalized blackbody temperature and the computed radiance.

Wavefront Measurements

There are a variety of techniques for measuring wavefront distortions.[15] In the past, for example, we have used shearing interferometers. A shearing interferometer is simply a dielectric plate that is tilted with respect to the incident wavefront (Fig. 8). Because of the second surface reflection, a replica of the incident wavefront is produced, but this replica is "sheared" or shifted laterally by an amount s that depends on the thickness L, refractive index n_s, and tilt θ of the dielectric plate. When this wavefront pair is detected by observation with a square-law device (detectors of optical radiation are said to be "square-law" because they respond to the square of the field), a series of fringes is produced. The local directional derivative of the wavefront can be inferred from these fringes. For example, a collimated beam produces no fringes (the derivative of a constant is zero), whereas a spherical wavefront produces an evenly spaced family of straight fringes.

The advantages of a shearing interferometer are that it is very inexpensive and the quality of the plate is unimportant. Since we are interested only in changes to some nominal wavefront induced by temperature gradients, the plate need not be particularly flat or even have parallel faces. Drawbacks to this approach are that calibration is problematic and interpretation of the fringe patterns is fairly numerically intensive. Processing involves a detection step in which the fringe pattern deviations are demodulated (much like the demodulation process that takes place in an AM radio) and a subsequent phase unwrapping step.[16] This latter step is necessary because the fringe patterns are modulo 2π, while the wavefront deviations can be many times this factor.

More recently, we have been measuring wavefront distortions using a Shack-Hartmann wavefront sensor[17] (Fig. 9). The principal components of the device are a lenslet array and a camera located near the focal plane of the lenslets. The wavefront to be analyzed is intercepted by the lenslet array, each member of which focuses a spot on the camera focal plane. Over the aperture of each lenslet, the wavefront will display an average tilt. This tilt is manifested in the focal plane as a lateral shift in the position of the focused spot. By determining the centroid of each of these spots, a matrix of wavefront slopes is built up. This is a very

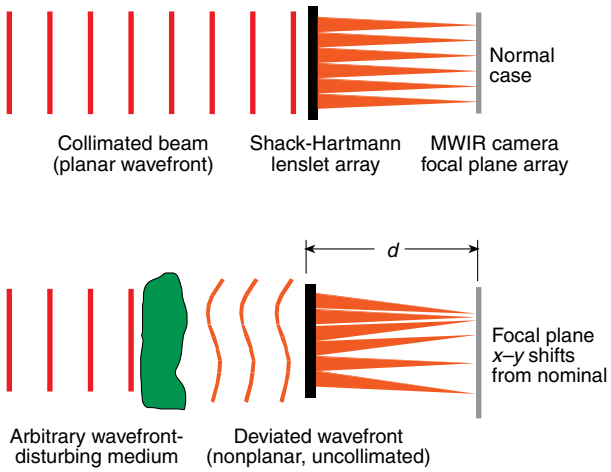

Figure 9. Principle of operation of a Shack-Hartmann wavefront sensor.

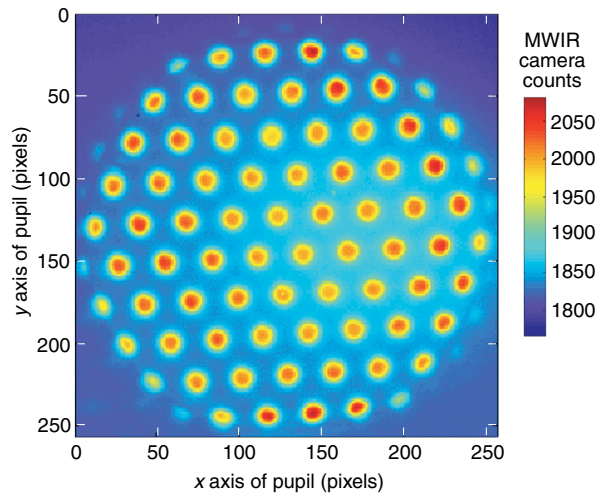

Figure 10. MWIR image produced by a lenslet array. The location of each focal spot is determined by a centroiding process.

robust measurement technique that is immune to vibration and provides the wavefront slope at temporal intervals determined by the frame time of the camera.

The particular lenslet array that we have been using (APH-Q-0.866-36.1, Advanced Microoptic Systems GmbH) is made of fused silica with an interelement spacing of 0.866 mm (hexagonal close-packing) and a focal length in the visible of 36.1 mm. Interestingly, calibration depends not so much on the focal length as on the actual distance from the lenslet array to the focal plane. The particular distance is not critical, but *knowledge* of the distance is. This distance can be established in a variety of ways. One is to simply tilt the sensor by a known angle, say α. The distance from the lenslet array to the focal plane is then given by $D/\tan\alpha$, where D is the measured lateral shift in the focal spots. We chose to use an equivalent method of tilting the incoming wavefront by a known amount using a wedge prism.

An interesting feature of the Shack-Hartmann sensor is that the angular resolution is much finer than the pixel size divided by the focal length. Rather, if one uses a centroiding technique to assess the focal spot movements, the precision more directly depends on the number of gray levels in the camera image. A typical focal plane pattern for the lenslet array is shown in Fig. 10. During an actual test measurement, the individual focal spots are seen to move in response to the wavefront distortions.

NUMERICAL AND THEORETICAL TOOLS

Numerical and theoretical tools provide a predictive capability. Specifically, ATLAS predicts temperature distributions based on thermal load predictions from the empirically based engineering model, and mechanical effects are modeled using finite-element concepts (NASTRAN). Code development in ATLAS and NASTRAN and the subsequent predictions are provided at APL by the Mechanical and Aeronautical Engineering Group. Optical effects due to these heating and deformation patterns are provided by closed-form analytic approximations and by numerical ray traces using OSLO SIX (a commercial design software package from Sinclair Optics, Inc.) in the Electro-Optical Systems Group.

ATLAS/NASTRAN

As noted earlier, an empirically based engineering model is used to estimate the aerodynamically generated heat loads on the surface of a window. Subsequently, ATLAS estimates the volumetric temperature distributions. Pyrometric measurements provide an experimental alternative to the use of the engineering model. Such would be the approach for wind tunnel or laser heating tests.

Next, these temperatures must be incorporated into a model that describes the temperature of the entire volume of the window, not just the surface. As an example, a sapphire dome typically is modeled as six concentric layers of facets from the outer to inner surface of the dome. Each layer consists of 944 nodal points that create a total of 914 facets. The IR pyrometric data are used to specify the temperatures of the 914 facets on the exterior of the dome. ATLAS, using all frames of surface facet temperature data from a particular test run, creates a volume temperature profile of the dome versus time. This volumetric thermal model is used as input to NASTRAN, which then calculates stresses and strains within the window. For selected key times during the test, the ATLAS volumetric thermal data and the NASTRAN deformation data are used as inputs to a ray trace simulation that numerically models the heated, deformed dome.

Ray Trace Predictions Using OSLO

OSLO SIX allows the user to input a complex optical system prescription, to trace rays, and to compute

A PERTURBATION SOLUTION TO THE EIKONAL EQUATION

Consider a dielectric slab of thickness d and inhomogeneous refractive index $n(x, y, z)$ surrounded by a homogeneous material of refractive index n_0, as shown in the figure. The trajectory of a ray in the material, where the ray enters the material at an angle θ_0 with respect to the surface normal at the point $(x_0, y_0, 0)$, is governed by the eikonal equation,

$$\frac{d^2x}{dz^2} = \frac{1}{n}\left[1 + \left(\frac{dx}{dz}\right)^2 + \left(\frac{dy}{dz}\right)^2\right]\left(\frac{\partial n}{\partial x} - \frac{dx}{dz}\frac{\partial n}{\partial z}\right)$$

$$\frac{d^2y}{dz^2} = \frac{1}{n}\left[1 + \left(\frac{dx}{dz}\right)^2 + \left(\frac{dy}{dz}\right)^2\right]\left(\frac{\partial n}{\partial y} - \frac{dy}{dz}\frac{\partial n}{\partial z}\right),$$

where we have chosen to parameterize the transverse coordinates (x, y) in terms of the longitudinal z.

For n homogeneous, the ray follows the straight line, $x = x_0 + x_1 z$, $y = y_0 + y_1 z$, and emerges at $z = d$ parallel to the incident ray. We define the angular deviation (from parallelism with the incident ray) of this exiting ray by $\delta\theta_r$. Obviously, for the homogeneous case, $\delta\theta_r = 0$. The coefficients x_1 and y_1 can be obtained by applying Snell's law within the "plane of incidence" (here, the y–z plane).

In the inhomogeneous case, we write $n(x, y, z)$ in the form of a Taylor series expansion about the incident point:

$$\begin{aligned} n(x, y, z) = {} & [n_{000} + n_{010}(x - x_0) + n_{001}(y - y_0) + \ldots] \\ & + z[n_{100} + n_{110}(x - x_0) + n_{101}(y - y_0) + \ldots] \\ & + \ldots . \end{aligned}$$

We seek a solution to the eikonal equation of the form

$$x = x_0 + x_1 z + x_2 z^2 + \ldots$$
$$y = y_0 + y_1 z + y_2 z^2 + \ldots$$

so that the trajectory generally is no longer a straight line. Substituting these trial solutions, together with the assumed form for n, allows one to calculate the coefficients $(x_j, y_j;\ j \geq 2)$ in terms of the various coefficients which appear in the assumed form for $n(x, y, z)$. These coefficients have simple interpretations. For example, n_{001} represents the value of $\partial n/\partial y$ evaluated at the incident point $(x_0, y_0, 0)$, n_{100} represents $\partial n/\partial z$ evaluated at $(x_0, y_0, 0)$, etc. After some algebra, one finds that to first order in d, the ray angular deviation takes the form

$$\delta\theta_r = d\left\{\frac{n_{001}}{n_0 \cos\theta_0\left[1 - \left(\frac{n_0}{n_{000}}\sin\theta_0\right)^2\right]^{1/2}}\right\}.$$

Note that $\delta\theta_r$ is proportional to n_{001}, which is given by the initial rate of change of n at the point $z = 0$ within the plane of incidence, as shown in the figure. Since we may write

$$\nabla n = \frac{dn}{dT}\nabla T,$$

where T is the temperature, we see that the ray angular deviation to this order of approximation is proportional to the temperature gradient at the point $z = 0$ within the plane of incidence. In other words, the ray angular deviation is proportional to the *surface* temperature gradient!

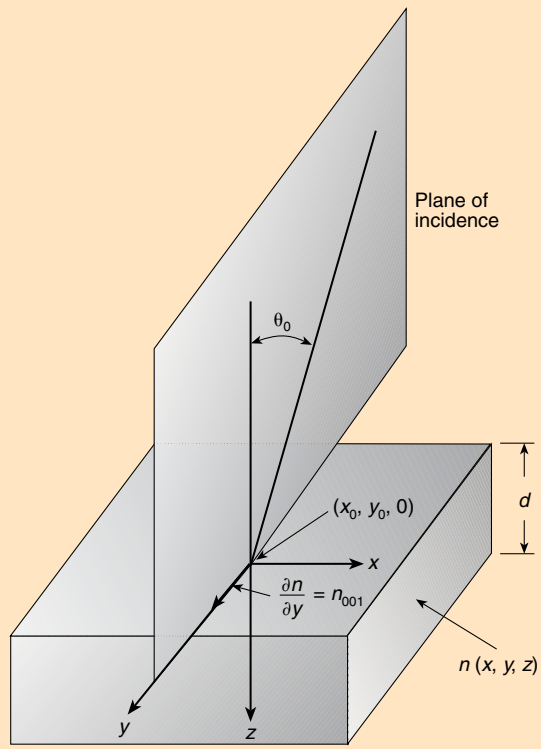

various performance metrics (e.g., point spread function, modulation transfer function, encircled energy, distortion). ATLAS volumetric thermal data and NASTRAN deformation data of the sapphire dome at an instant in time can be included in this prescription. The deformations of the outer and inner surfaces of the dome cause them to deviate from spherical, thus altering the angle of incidence at the air/sapphire interface. This causes ray deviation from nominal, which is evident at the output of the system. The thermal variation throughout the thickness of the dome results in a refractive index gradient (described in the following sections) that causes curvature of the ray trajectories. Ray deviations caused by the heated, deformed sapphire dome

are manifested at the image plane as blur and centroid shifts. For a nonuniformly heated dome these effects depend on the portion of the dome through which the imaging telescope is looking.

Analytic Approximations to Ray Tracing

As discussed previously, there are two effects of nonuniform heating that we need to consider: (1) nonuniform heating of the window material causes a physical deformation, and (2) the temperature gradient causes a spatial variation in the refractive index of the material.

If one begins with Maxwell's equations that describe the spatial and temporal behavior of electromagnetic fields and makes the short-wavelength approximation (wavelength is much smaller than any physical structure that the field may experience), then one can arrive at what is known as the eikonal equation.[9] This is a simple differential equation that describes the propagation of a ray of light within a generalized medium in which the refractive index may vary with position.

The more sophisticated ray trace codes are capable of describing propagation through gradient index of refraction (GRIN) media. As noted earlier, the temperature distribution within the window is estimated numerically. As a result, the ray trace through the resulting GRIN medium is computationally intensive; the eikonal equation must in effect be solved locally and repeatedly.

So what is the problem with this approach? It is that these numerically intensive predictions provide little insight into the physics of the problem. Instead, we attempt to find an approximate solution to the eikonal equation within a GRIN medium. Our approach uses a perturbational technique; we assume that the effect we are treating is a small variation on the overall behavior of the ray. This allows an analytic approximation (see the boxed insert) which predicts that the principal effect is due to the temperature gradient *on the dielectric interface* rather than the temperature gradient into the medium. As an example, Fig. 11 shows a comparison of the graded index ray deviations derived from first- and second-order analytic models,[18] as well as the angular deviation calculated via the OSLO ray trace program. As seen here, the second-order approximation shows excellent agreement with the ray trace predictions. These results illustrate the benefit provided by approximate solutions. Although the numerical and analytical results are very similar, the fact that the ray deviation depends on the surface temperature gradient is not elucidated by the numerical ray trace.

RESULTS

Here we detail some recent results of efforts to validate ray trace and stress estimates. These tests took place in the Laser Hardened Materials Evaluation Laboratory (LHMEL) at Wright-Patterson Air Force Base, Dayton, Ohio. At LHMEL we demonstrated that CO_2 laser radiation heating of a sapphire dome could simulate the aerodynamic heating produced by supersonic flight while allowing a complete set of noninvasive diagnostic tools to be used. Important optical testing of nonuniformly heated missile domes was conducted without using a wind tunnel, thus improving the measurement precision while reducing test cost.

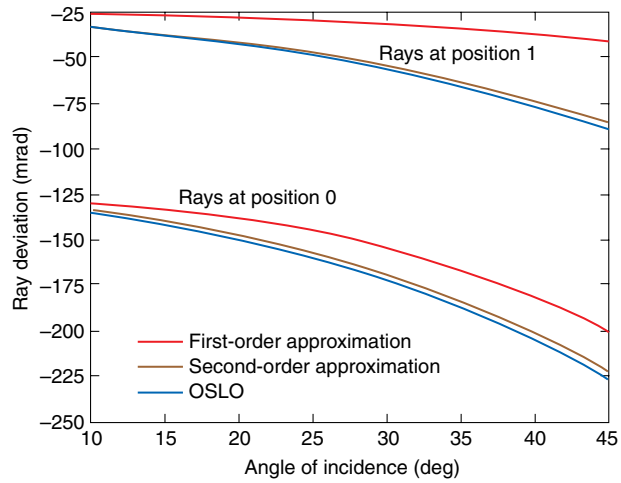

Figure 11. Comparison of first-order, second-order, and OSLO computations of ray deviation.

Experimental Validation of Ray Deviations

The most recent measurements were performed on a sapphire dome. Figure 12 is a photograph of such a dome

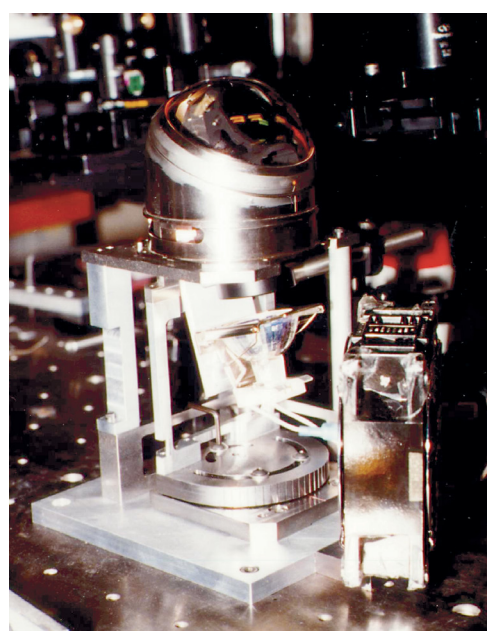

Figure 12. Mounted dome with focal plane illumination.

atop a test fixture. In the standard optical layout, a collimated beam enters the sapphire dome, passes through a corrector lens (to correct for aberrations introduced by the dome), continues through telescope optics, and then is imaged at a focal plane array (Fig. 13). For the LHMEL tests, the configuration was reversed from the standard optical layout, with an incandescent light source illuminating a pinhole replacing the focal plane array of the seeker. The rays from this point source proceed through the telescope optics and the corrector, and exit the system through the heated, deformed sapphire dome as a nearly collimated bundle of rays with diameter D_1. Relay optics consisting of a spherical mirror and a CaF_2 lens were used to shrink the diameter of this beam down to the diameter of the lenslet array, D_2 (Fig. 14). An additional benefit of this spatial demagnification was the concomitant angular magnification,[19] which increased the sensitivity of the measurement. Finally, the MWIR focal plane array was placed a short distance d from the lenslet array to detect any wavefront deviation.

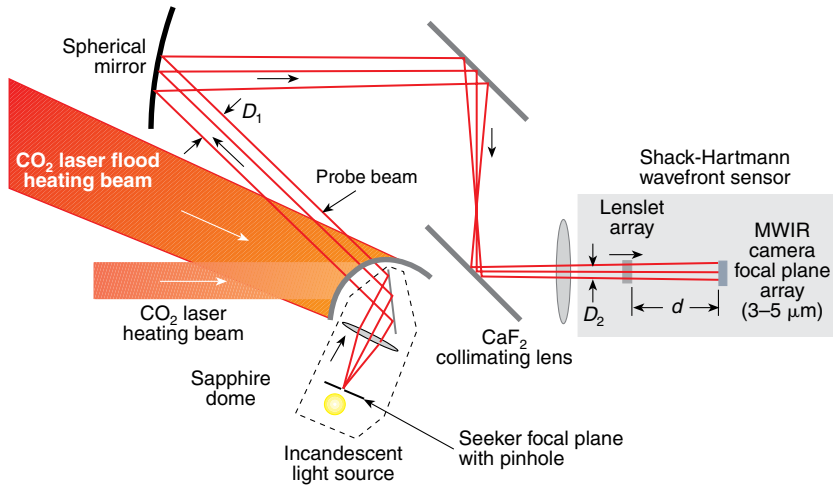

Figure 14. Schematic of the measurement configuration at LHMEL.

Wavefront distortion data were obtained for various sensor look angles, which allowed investigation of the effects of the gimbaled sensor looking through different portions of the heated dome. For each run, data were collected for several seconds before the start of heating, during the 4 s of laser heating, and for several additional seconds after the end of heating. Imaging pyrometry provided estimates of the surface temperature of the dome during these tests.

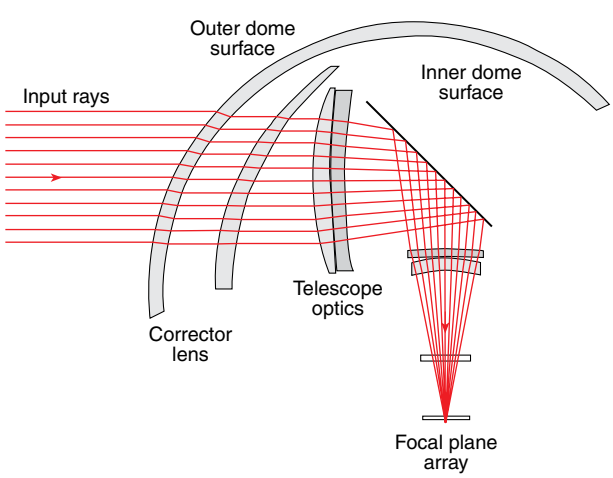

Figure 13. Example optical layout of an imaging telescope with a dome.

After processing the data from the MWIR (wavefront distortion) and LWIR (imaging pyrometry) cameras, the wavefront slope maps were superimposed on their corresponding thermal contour maps at particular times for each data run. Figure 15 shows typical results, with the wavefront slope arrows scaled to their maximum value (in this case, 0.793 mrad). As expected, the magnitude of the wavefront distortion was small near the center of the hot spot (where the temperature was nearly constant) and large in areas of high thermal gradients. For the various data runs, the maximum wavefront deviation over the pupil ranged from 0.5 to 0.8 mrad.

It is also instructive to examine the temporal evolution at a particular spatial location on the dome. The spatial temperature gradient produces a spatial gradient in the index of refraction, which causes the rays exiting the surface of the dome to bend. Therefore, there should be a direct correlation between the wavefront deviation and the temperature gradient produced by laser heating. The wavefront deviation and temperature gradient during heating (0–4 s) and cooling (4–10 s) are plotted together as functions of time in Fig. 16. This shows that nonuniform laser heating of the dome affects the wavefront slopes as expected.

Experimental Validation of Stress Estimates

In addition to wavefront analysis, measurements of the full-field stress distributions in a laser-heated sapphire disk also were performed at LHMEL. For these measurements, a 725-W CO_2 laser was used to heat a 3.2-cm circular section of a sapphire disk. As explained previously, the laser heating caused localized expansion (strain), resulting in a circular stress distribution in the sapphire. The laser heating was applied for 4 s, and the stress distributions were monitored using a linear polariscope. Shown in Fig. 17 is a comparison of the thermal and photo-elastic images after

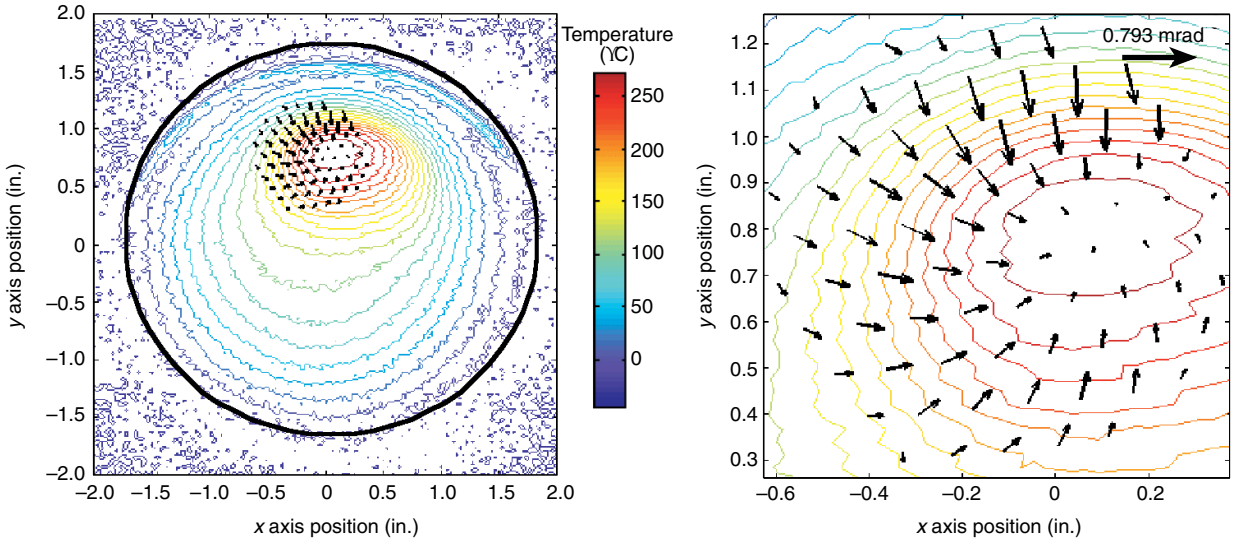

Figure 15. Example thermal contour map superimposed on a corresponding wavefront slope map (left), and an enlarged view of the pupil area (right).

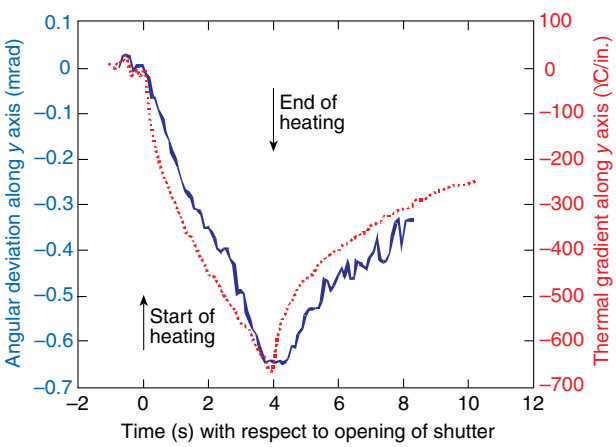

Figure 16. Angular deviation and temperature gradient during heating and cooling.

4 s of laser heating. A cut through the center of the two images clearly shows that the greatest stress differences are found at the steepest thermal gradient, with four stress-induced fringes clearly visible.

Estimates of the relative stress differences $\Delta\sigma$ can be calculated from

$$\Delta\sigma = \frac{\lambda}{2Lc}(2m+1), \quad m = 0,1,\ldots, \tag{10}$$

where m is the fringe order, λ is the laser wavelength (632.8 nm), L is the thickness of the disk (2.54 mm), and c is a relative stress–optic constant. Equation 10 is used to calculate the principal stress differences at the two fringes. A plot of these principal stress differences calculated using ATLAS and NASTRAN is shown in

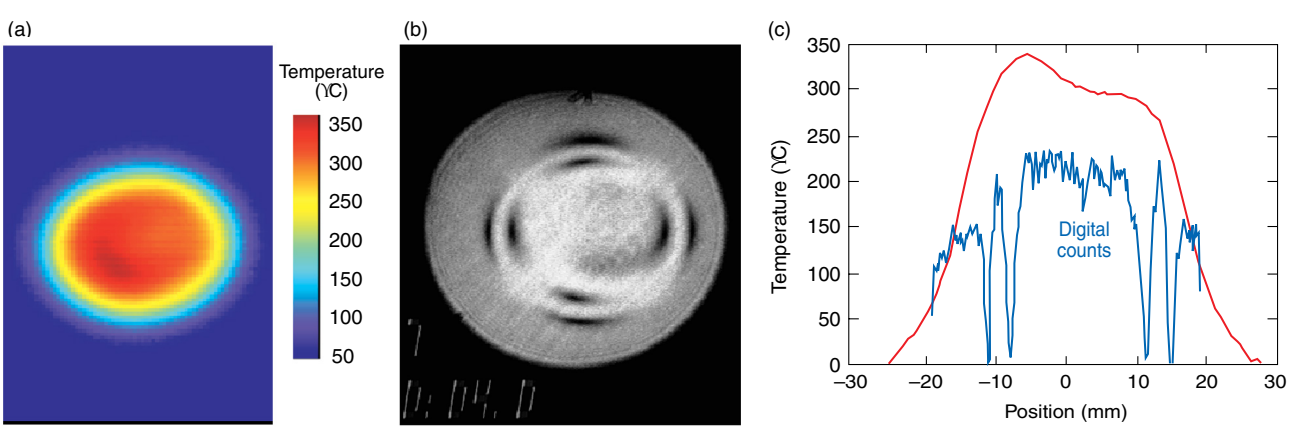

Figure 17. Comparison after 4 s of laser heating of a sapphire disk: (a) temperature image, (b) photo-elastic image, and (c) linescan through the temperature and photo-elastic image.

Fig. 18, using a normalized scale. Overlaid on this plot is the spatial location of the two fringes, along with the measured stress difference values. As seen here, there is excellent agreement between the theoretical and experimental values.

CONCLUSIONS

Figure 19 summarizes the experimental validation efforts discussed herein. A high-energy laser is used to impress heating profiles in a sapphire dome, which is a component of an imaging sensor. These profiles are intended to be representative of the nonuniform aerothermal heating produced by hypersonic flight. Concomitantly, a number of diagnostic measurements are performed. Imaging pyrometry provides a quantitative estimate of the surface temperatures on the dome; interferometric measurements yield information on distortions of the wavefront transmitted through the nonuniformly heated dome. Full-field stress measurements are currently performed on sapphire plates and planned for the dome. Although not yet performed, actual deformation of the dome can be measured using speckle techniques.[20]

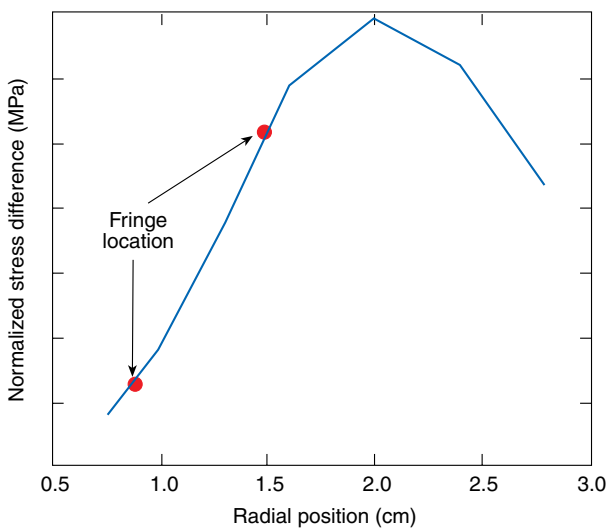

Figure 18. NASTRAN calculation and photo-elastic measurement of principal stress differences.

Pyrometric measurements provide estimates of temperature distributions that are input to ATLAS. Outputs from ATLAS, in turn, are input to NASTRAN and OSLO. NASTRAN provides estimates of stress and deformation. Photo-elastic measurements lead to estimates of stress that can be compared directly with these predictions. For estimates of ray bending, OSLO also requires input data on deformations that are provided by NASTRAN. Such wavefront estimates are compared with the wavefront measurements performed by shearing interferometry or Shack-Hartmann tests. Deformation measurements will allow for experimental validation of NASTRAN estimates. Finally, deformation and temperature measurements will provide data to be input to our analytic ray trace codes. These algorithms will generate estimates of wavefront distortions that can be compared with those estimated using OSLO and those measured during the tests.

The ultimate aim of all these efforts is a simple, physics-based, parametric model of the optical performance of aerodynamically heated windows. Our success thus far has resulted from the contributions of a variety of people having diverse talents. As we have shown, however, it is not the result of a single unified effort. Rather, it represents the convergence of several separate studies, some abstract and some applied. As such, it is a true illustration of the synergistic roles of fundamental research and development.

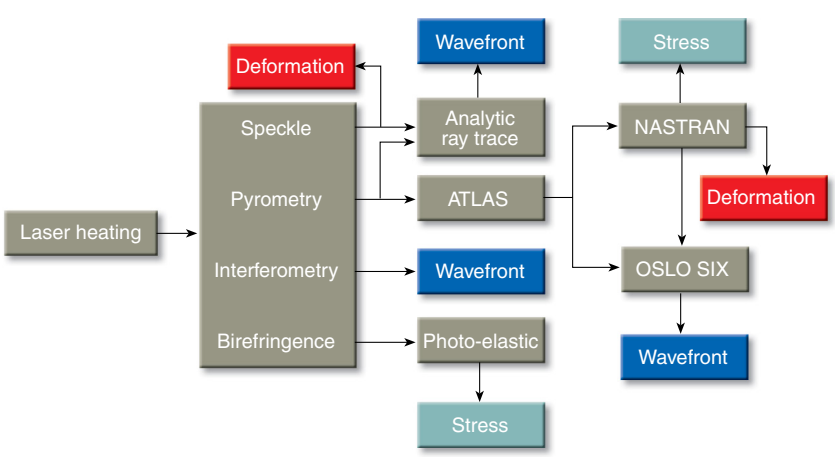

Figure 19. Details of the model validation process.

REFERENCES

[1]Walters, R. H., *User's Guide to the Aerothermal Loads and Stresses Program*, AM-96-E02, JHU/APL, Laurel, MD (Feb 1997).

[2]Reymond, M., and Miller, M. (eds.), *MSC/NASTRAN Quick Reference Guide Version* 68, The MacNeal-Schwendler Corp. (1994).

[3]Scruby, C. B., and Drain, L. E., *Laser Ultrasonics: Techniques and Applications*, Adam-Hilger, New York (1990).

[4]Wagner, J. W., "Optical Detection of Ultrasound," in *Physical Acoustics*, Vol. 19, W. P. Mason and A. D. Pierce (eds.), Academic Press, New York, pp. 201–266 (1990).

[5]Nye, J. F., *Physical Properties of Crystals: Their Representation by Tensors and Matrices*, Clarendon Press, Oxford (1992).

[6]Goto, T., Andersen, O. L., Ohno, I., and Yamamoto, S., "Elastic Constants of Corundum up to 1825 K," *J. Geophys. Res.* **94**(86), 7588–7602 (1989).

[7]Klocek, P., *Handbook of IR Optical Materials*, Marcel Dekker, New York (1991).

[8]Blodgett, D. W., and Baldwin, K. C., "Elastic Moduli and Defect Orientation Studies

of Aspen-Treated Sapphire Using Laser Ultrasonics," in *Proc. 8th DoD Electromagnetic Windows Symp.*, pp. 83–92 (2000).
[9]Born, M., and Wolf, E., *Principles of Optics*, 6th Ed., Pergamon Press, New York (1989).
[10]Rastogi, P. C. (ed.), *Optical Measurement Techniques and Applications*, Artech House, Boston (1997).
[11]Sova, R. M., Linevsky, M. J., Thomas, M. E., and Mark, F. F., "High-Temperature IR Properties of Sapphire, AlON, Fused Silica, Yttria, and Spinel," *IR Phys. Technol.* **99**, 251–261 (1998).
[12]Thomas, M. E., Wayland, P. S., and Terry, D. H., "Imaging Pyrometry of Oxides," in *Proc. SPIE-Thermosense* XX , Vol. 3361, pp. 2–13 (Apr 1998).
[13]Terry, D. H., Thomas, M. E., Linevsky, M. J., Prendergast, D. T., Bagford, J. O., and Lander, M. L., "Imaging Pyrometry of Laser-Heated Sapphire," in *Proc. 7th DoD Electromagnetic Windows Symp.*, JHU/APL, Laurel, MD, pp. 264–276 (May 1998).
[14]Terry, D. H., Thomas, M. E., Linevsky, M. J., and Prendergast, D. T., "Imaging Pyrometry of Laser-Heated Sapphire," *Johns Hopkins APL Tech. Dig.* **20**(2), 162–169 (1999).
[15]Malacara, D., *Optical Shop Testing*, John Wiley and Sons, New York (1978).
[16]Ghilia, D. C., and Pritt, M. D., *Two-Dimensional Phase Unwrapping: Theory, Algorithms, and Software*, John Wiley & Sons, Inc., New York (1998).
[17]Geary, J. M., *Introduction to Wavefront Sensors*, SPIE Optical Engineering Press, Bellingham, WA (1995).
[18]Joseph, R. I., and Thomas, M. E., *Extension of Previous Analytic Results for Ray Angular Deviation in a Hemispherical Shell of Inhomogeneous Refractive Index*, A1F(5)99-U-089, JHU/APL, Laurel, MD (5 Oct 1999).
[19]Smith, W. J., *Modern Optical Engineering: The Design of Optical Systems*, McGraw-Hill, New York (1966).
[20]Joenathan, C. "Speckle Photography, Shearography, and ESPI," Chap. 6 in *Optical Measurement Techniques and Applications*, P. K. Rastogi (ed.), Artech House, Inc., Boston (1997).

ACKNOWLEDGMENTS: We gratefully acknowledge the aid of John Bagford of Anteon Corp., test director of LHMEL. Also recognized is Simon Kaplan for his cooperation during the index of refraction measurements at NIST. Brian Kemp (A1C) provided the ATLAS and NASTRAN predictions used in the LHMEL data analysis.

THE AUTHORS

DONALD D. DUNCAN, a member of APL's Principal Professional Staff, received his Ph.D. in electrical engineering from Ohio State University in 1977. He is an Associate Professor of Ophthalmology at the Johns Hopkins School of Medicine and a lecturer in the JHU School of Continuing Education. From 1977 to 1983, Dr. Duncan worked as a senior analyst at the Pacific-Sierra Research Corporation in Santa Monica, California, conducting research in optical propagation through aerosol media and turbulence. He joined APL in 1983 and works on research projects in optics and biomedical engineering. He is Supervisor of the Phenomenology and Measurements Section in ADSD's Electro-Optical Systems Group. His e-mail address is donald.duncan@jhuapl.edu.

KEVIN C. BALDWIN received B.S. and M.S. degrees in optics in 1990 and 1991, respectively, from the University of Rochester; an M.S. in electrical engineering in 1993 from the Rochester Institute of Technology; and an M.S.E. in 1994 and a Ph.D. in 1998, both in electrical engineering, from The Johns Hopkins University. In 1998 Dr. Baldwin joined ADSD's Electro-Optical Systems Group and has worked on many projects ranging from the use of deformable contours for the segmentation of biomedical images to the design of low F/# optics for use in long-wave infrared seekers. Currently, he is involved in the modeling, development, and testing of several underwater imaging systems. His e-mail address is kevin.baldwin@jhuapl.edu.

DAVID W. BLODGETT is a materials scientist in APL's Electro-Optical Systems Group in the Air Defense Systems Department. He received a B.S.E.E. from Purdue University in 1991 and M.S. and Ph.D. degrees from The Johns Hopkins University in 1995 and 1998, respectively. His current research interests center on the use of near-field optics, conventional optics, and laser-generated ultrasonics for characterizing the mechanical and optical properties of optical window materials. His e-mail address is david.blodgett@jhuapl.edu.

MICHAEL J. ELKO received B.S. and M.Eng. degrees in applied and engineering physics from Cornell University in 1989 and 1991, respectively. He was employed at APL from 1991 to 2000 and was a member of the Senior Professional Staff working as an optical engineer in ADSD's Electro-Optical Systems Group. While at APL, he was involved in the design, test, analysis, calibration, and simulation of numerous optical instruments. He worked on a variety of projects including MSX, the NEAR Multi-Spectral Imager, SM-2 Block IV-A, SM-3, and the Low Cost Gun Launched Seeker. He is currently employed by CENiX Inc., in Allentown, Pennsylvania, where he is designing next-generation fiber-optic telecommunication devices. His e-mail address is melko@CENiXInc.com.

RICHARD I. JOSEPH received a B.S. from the City College of the City University of New York in 1957 and a Ph.D. from Harvard University in 1962, both in physics. From 1961 to 1966, he was a senior scientist with the Research Division of the Raytheon Co. Since 1966, Dr. Joseph has been with the Department of Electrical and Computer Engineering of The Johns Hopkins University, where he is currently the Jacob Suter Jammer Professor of Electrical Engineering. During 1972, Dr. Joseph was a Visiting Professor of Physics at Kings College, University of London, on a Guggenheim Fellowship. A member of APL's Principal Professional Staff, his research interests include electromagnetic theory, statistical physics, applied optics, and photonics. Dr. Joseph is a Fellow of the American Physical Society. His e-mail address is rjoseph@ece.jhu.edu.

MARK J. MAYR is Supervisor of the Electro-Optical Systems Group in the Air Defense Systems Department and a member of APL's Principal Professional Staff. He received a B.S.E.E. from the Milwaukee School of Engineering in 1978 and an M.S.E.E. from The Johns Hopkins University in 1981. Mr. Mayr has extensive experience in the design, analysis, testing, and model validation of infrared and electro-optical sensors and systems as well as a related background in inertial and control systems. He has been the lead engineer for a variety of IR, UV, and visible sensors and systems on missiles and spacecraft. He has also developed instrumentation for laser pointing and tracking systems and submarine applications, among others. Mr. Mayr is a member of the Society of Photo-Optical Instrumentation Engineers. His e-mail address is mark.mayr@jhuapl.edu.

DANIEL T. PRENDERGAST joined APL in 1985 as an engineer in the Electro-Optical Systems Group in the Air Defense Systems Department and is a member of APL's Senior Professional Staff. He received a B.F.A. from the Columbus College of Art and Design in 1978 and a B.S. in electrical engineering from The Ohio State University in 1985. Since joining APL, Mr. Prendergast has worked on the optical test and evaluation of infrared missile seekers as well as the calibration and development of optical test facilities. His work includes calibrating and aligning optical systems on the MSX and NEAR spacecraft. His e-mail address is daniel.prendergast@jhuapl.edu.

DAVID H. TERRY received B.S.E.E. and M.S.E. degrees from The Johns Hopkins University. He is a member of APL's Senior Professional Staff and an engineer in ADSD's Electro-Optical Systems Group. Since joining APL in 1987, he has worked on a variety of tasks that include neural network ship classification, a multi-aperture optical correlator, and the calibration of MSX spacecraft optical sensors. Currently he is working on infrared imaging, including pyrometry of infrared windows and remote sensing of TBM intercepts. He is also lead engineer for APL's Rolling Airframe Missile's infrared systems engineering efforts. His e-mail address is david.terry@jhuapl.edu.

MICHAEL E. THOMAS received a B.E.E. degree from the University of Dayton and M.S. and Ph.D. degrees from Ohio State University. Since joining APL in 1979, he has been working on electromagnetic propagation, optical properties of materials, and remote sensing. In 1982, he was a postdoctoral fellow in the Department of Physics at the Naval Postgraduate School. In 1988, Dr. Thomas became a faculty member of the G.W.C. Whiting School of Engineering in the Part-Time Programs in Engineering and Applied Science, teaching courses on optical propagation and lasers. In 1998, he was appointed Research Professor in the Department of Electrical and Computer Engineering at The Johns Hopkins University. His current research interests include experimental and theoretical modeling of atmospheric propagation in the infrared, optical and infrared window materials, lidar modeling, and femto-second pulse propagation. Dr. Thomas is a fellow of the Optical Society of America. His e-mail address is michael.thomas@jhuapl.edu.

SUZANNE C. WALTS is an Associate Professional Staff engineer in the Electro-Optical Systems Group in the Air Defense Systems Department. She received a B.S. in physics from Wake Forest University in 1997 and an M.S. in electrical engineering from the University of Michigan in 1999. Since joining APL in 1999, she has been involved with measurements, data analysis, and modeling for various systems. Her research interests focus on materials characterization with optical methods. Her e-mail address is suzanne.walts@jhuapl.edu.